JACS
JOURNAL OF THE AMERICAN CHEMICAL SOCIETY
Article
Cite This: J. Am. Chem. Soc. 2019, 141, 6658−6671
pubs.acs.org/JACS

The *Trans* Effect in Electrocatalytic CO_2 Reduction: Mechanistic Studies of Asymmetric Ruthenium Pyridyl-Carbene Catalysts

Sergio Gonell,[‡] Marsha D. Massey,[‡] Ian P. Moseley,[‡] Cynthia K. Schauer,[‡] James T. Muckerman,[§] and Alexander J. M. Miller*[,‡]

[‡]Department of Chemistry, University of North Carolina at Chapel Hill, Chapel Hill, North Carolina 27599-3290, United States
[§]Chemistry Division, Brookhaven National Laboratory, P.O. Box 5000, Upton, New York 11973-5000, United States

Supporting Information

ABSTRACT: A comprehensive mechanistic study of electrocatalytic CO_2 reduction by ruthenium 2,2′:6′,2″-terpyridine (tpy) pyridyl-carbene catalysts reveals the importance of stereochemical control to locate the strongly donating N-heterocyclic carbene ligand *trans* to the site of CO_2 activation. Computational studies were undertaken to predict the most stable isomer for a range of reasonable intermediates in CO_2 reduction, suggesting that the ligand *trans* to the reaction site plays a key role in dictating the energetic profile of the catalytic reaction. A new isomer of $[Ru(tpy)(Mebim\text{-}py)(NCCH_3)]^{2+}$ (Mebim-py is 1-methylbenzimidazol-2-ylidene-3-(2′-pyridine)) and both isomers of the catalytic intermediate $[Ru(tpy)(Mebim\text{-}py)(CO)]^{2+}$ were synthesized and characterized. Experimental studies demonstrate that both isomeric precatalysts facilitate electroreduction of CO_2 to CO in 95/5 MeCN/H_2O with high activity and high selectivity. Cyclic voltammetry, infrared spectroelectrochemistry, and NMR spectroscopy studies provide a detailed mechanistic picture demonstrating an essential isomerization step in which the *N-trans* catalyst converts in situ to the *C-trans* variant. Insight into molecular electrocatalyst design principles emerge from this study. First, the use of an asymmetric ligand that places a strongly electron-donating ligand *trans* to the site of CO_2 binding and activation is critical to high activity. Second, stereochemical control to maintain the desired isomer structure during catalysis is critical to performance. Finally, pairing the strongly donating pyridyl-carbene ligand with the redox-active tpy ligand proves to be useful in boosting activity without sacrificing overpotential. These design principles are considered in the context of surface-immobilized electrocatalysis.

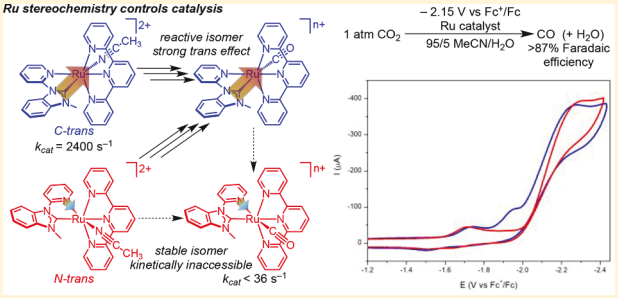

INTRODUCTION

Carbon dioxide holds immense promise as a sustainable feedstock for the synthesis of energy-dense fuels. Electrochemical CO_2 reduction has received particular interest,[1−7] based in part on the promise of coupling electrocatalysts with renewable energy sources such as solar or wind power.[8−12] The development of CO_2 reduction electrocatalysts faces an inherent challenge in selectivity; however, a catalyst must exhibit kinetic selectivity for one of the various thermodynamically accessible carbon-based products while also avoiding undesirable proton reduction to H_2. Ideal catalysts should also maintain high activity with long-term stability.

Ruthenium polypyridine complexes (Figure 1) serve as a prime example of the evolution of molecular electrocatalysts toward improved selectivity and stability through structural redesign.[13,14] Early $[Ru(bpy)_2(CO)_2]^{2+}$ (bpy = 2,2′-bipyridine) catalysts, featuring a single type of chelating ligand,[15,16] produced mixtures of CO and formate in most cases and suffered from electropolymerization through bpy dissociation (although the resulting films remained electroactive).[17,18] Installation of a 2,2′:6′,2″-terpyridine (tpy) ligand to form $[Ru(tpy)(bpy)(L)]^{2+}$ prevented electropolymerization.[19−24] Further elaboration to replace bipyridine with the asymmetric organometallic bidentate 1-methylbenzimidazol-2-ylidene-3-(2′-pyridine) (Mebim-py) ligand furnished $[Ru(tpy)(Mebim\text{-}py)(L)]^{2+}$, which is a substantially faster electrocatalyst that

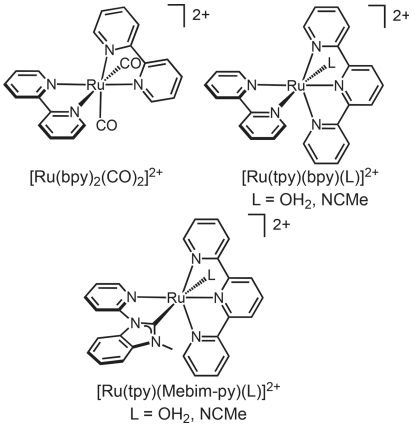

Figure 1. Ru polypyridine catalysts.

Received: February 14, 2019
Published: April 11, 2019

DOI: 10.1021/jacs.9b01735
J. Am. Chem. Soc. 2019, 141, 6658−6671

also boasts high selectivity for CO in acetonitrile solution[20] and tunable CO/H_2 ratios in water.[25] This is also a rare example of a molecular catalyst that is capable of both CO_2 reduction and water oxidation.[26] Recently, a Ru bipyridine complex fitted with large mesityl substituents successfully avoided electropolymerization to achieve rapid and selective CO_2 electroreduction to CO (k_{obs} = 1300 s^{-1}).[27]

The leading Ru electrocatalysts for CO_2 reduction feature multiple supporting ligands and low molecular symmetry, raising the possibility of intermediates that can adopt multiple geometric isomers. The aforementioned catalyst $[Ru(tpy)(Mebim\text{-}py)(NCCH_3)]^{2+}$, in particular, caught our attention. The asymmetric Mebim-py ligand can, in theory, support two stereoisomers that would likely exhibit significant reactivity differences. The viability of the various isomers during turnover was not explored in prior studies. Furthermore, the specific role of the strongly electron-donating carbene ligand in tuning reduction potentials or accelerating chemical reactions has not been elucidated, further motivating a detailed mechanistic study of this unique catalyst system.

The mechanistic diversity of ruthenium electrocatalysts is rather remarkable. Proposed pathways from CO_2 and a proton source to CO and H_2O are shown in Scheme 1.[5] Pathways A, B, and C all begin with two-electron reduction. In pathway A, CO_2 addition is followed by a *single protonation* to form a metallocarboxylic acid that undergoes electrochemical reduction before protonolysis releases water and forms a carbonyl complex. Rarely proposed for Ru complexes,[28] pathway A is observed in Mn and Re systems.[29,30] Pathway B, in which CO_2 binding is followed by *two sequential protonations* to form a carbonyl complex, is the mechanism proposed for most Ru catalysts, including $[Ru(bpy)_2(CO)(L)]^{2+}$ and $[Ru(tpy)(bpy)(L)]^{2+}$.[16,22] Pathway C involves protonation of a reduced species to form a metal hydride, which forms a formate complex by CO_2 insertion and finally undergoes a unique rearrangement to a metallocarboxylic acid to rejoin another pathway. The bulky precatalyst $Ru(Mes\text{-}bpy)(Cl)_2(CO)_2$ was proposed to operate via pathway C.[27] In pathway D, only a single one-electron reduction occurs before CO_2 addition; subsequent reduction generates the same metallocarboxylate intermediate in pathways A and B. Modification of the bidentate ligand on Ru-tpy-based catalysts led to a change in mechanism from pathway B to pathway D.[23,31] A similar ECE mechanism is observed in the formation of a carbonyl complex upon electrochemical reduction of $[CpRu(bpy)(NCCH_3)]^+$ under CO_2.[32]

Scheme 1. Mechanistic Pathways Proposed for Electrochemical Reduction of CO_2 to CO by Ru Electrocatalysts

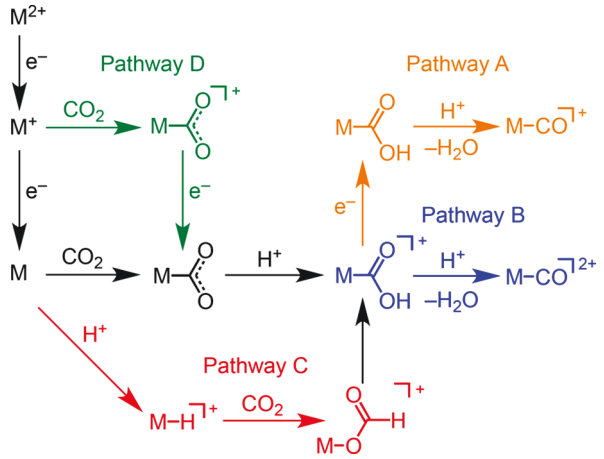

The first detailed mechanistic study of CO_2 reduction by pyridyl-carbene-supported Ru electrocatalysts is described here. DFT predictions of the relative stability of isomeric CO_2 electroreduction intermediates inspired the synthesis of *cis* and *trans* isomers of proposed catalytic intermediates, which were then characterized in detail using cyclic voltammetry and infrared spectroelectrochemical experiments. These studies establish the pyridyl-carbene catalyst system as a highly active and selective electrocatalyst that provides several significant lessons in electrocatalyst design. First, the asymmetric pyridyl-carbene ligand can adopt a geometry that places a strong σ-donor *trans* to the CO_2 activation site, leading to geometry-specific rate acceleration. Second, controlling the isomer structures along the mechanistic pathway proves critical for sustained activity. Finally, the catalyst teaches that the redox-active terpyridine ligand can control the catalytic onset potential, while the strongly donating, redox-inactive pyridyl-carbene chelate controls the rate of key chemical steps. This method of decoupling electronic tuning of nucleophilicity and redox potentials could be a valuable strategy for breaking "scaling relationships" by increasing the rate of chemical steps without increasing overpotential.

RESULTS AND DISCUSSION

Computational Investigation of Geometric Isomers.

Density functional theory (DFT) as implemented in the Gaussian 09 software package[33] was employed to estimate the relative stability of *C-trans* and *N-trans* isomers of plausible catalytic intermediates (Scheme 2). The *C-trans* stereochemistry is defined as the carbene donor sitting *trans* to the monodentate ligand binding site, while the *N-trans* stereochemistry is defined as the pyridine donor sitting *trans* to the monodentate ligand binding site. The B3LYP functional[34] was employed along with the cep-121g basis set[35,36] for Ru atoms

Scheme 2. Computational Study of the Relative Stability of Isomeric Structures

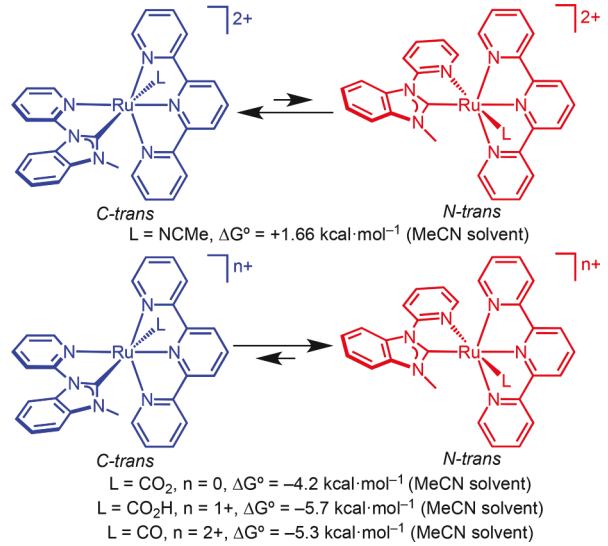

DOI: 10.1021/jacs.9b01735
J. Am. Chem. Soc. 2019, 141, 6658−6671

and the 6-31++G(d,p) basis set[37] for other atoms, with implicit solvation applied using the SMD method.[38]

Scheme 2 summarizes the relative free energies of *C-trans* and *N-trans* isomers for various complexes relevant to CO_2 electroreduction. The complexes of formula [Ru(tpy)(Mebim-py)(L)]$^{n+}$ are abbreviated **Ru-L**$^{n+}$, where L is a monodentate ligand, and assigned a prefix ***C***- or ***N***- denoting *C-trans* or *N-trans* stereochemistry, respectively. For the acetonitrile-bound precatalyst, the isomer with the NHC *trans* to the acetonitrile ligand, ***C*-Ru-MeCN**$^{2+}$, was computed to be more stable by 1.66 kcal/mol (MeCN solvent).

Surprisingly, all efforts to optimize the *N-trans* isomer of the key doubly reduced intermediate Ru(tpy)(Mebim-py) (***N*-Ru**^{0}) failed to converge on the targeted structure. Instead, the geometry shifted to a *C-trans* configuration (***C*-Ru**^{0}) during optimization. The spontaneous isomerization of the doubly reduced intermediate from *N-trans* to *C-trans* was explored further through a constrained optimization varying the angle between the tridentate and bidentate ligands (Figure 2). No minimum near the expected *N-trans* geometry was observed.

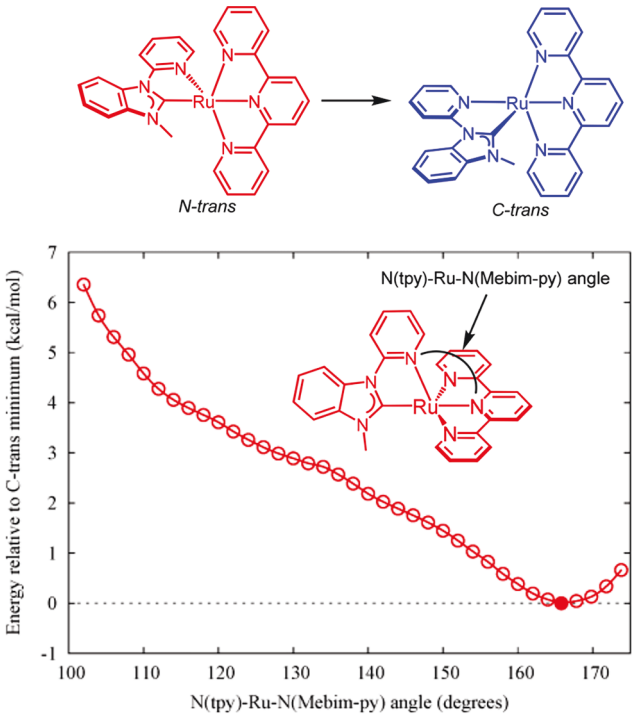

Figure 2. Variation of energy (relative to the minimum of ***C*-Ru**^{0}) as a function of the angle defined between the central tpy nitrogen atom and the Mebim-py pyridyl nitrogen atom (SMD water solvation model).

The highest occupied molecular orbitals (HOMOs) of five-coordinate singly reduced ***C*-Ru**$^+$ and doubly reduced ***C*-Ru**^{0} both show extensive delocalization across the Ru d-orbitals and the terpyridine π system, indicating significant terpyridine character in the reduction (Figure 3). The localization of electron density on terpyridine is noteworthy in the context of prior reports proposing that the related bipyridine complex Ru(tpy)(bpy) features one electron localized on tpy and another localized on bpy.[20,23] The Mebim-py ligand is expected to be very difficult to reduce, which may effectively force both reductions to involve the terpyridine ligand.

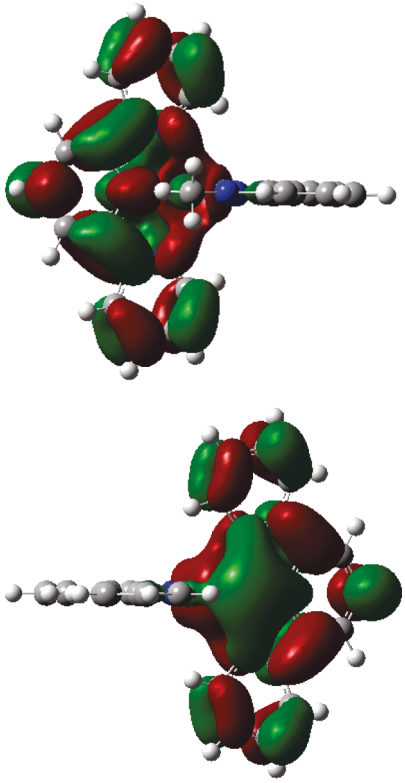

Figure 3. HOMO of ***C*-Ru**$^+$ (top) and ***C*-Ru**^{0} (bottom). The orbitals are almost identical; the complexes are depicted in different orientations to show both sides of the π system.

A change in isomer stability to favor *N-trans* is predicted for the closed-shell metallocarboxylate, metallocarboxylic acid, and carbonyl complexes. The computed isomer stability tracks with the expected *trans* influence of the ligands, with CO_2-derived ligands (strong *trans* influence) favored in a position *trans* to pyridine (weak *trans* influence). Isomers that orient two strong *trans* influence ligands (e.g., carbon donors) *trans* to each other are typically less stable than isomers that position strong and weak *trans* influence ligands across from each other. If the system is under thermodynamic control during catalysis, the catalyst would switch between *C-trans* and *N-trans* intermediates during each turnover. These computational predictions inspired us to isolate each isomer and examine the mechanism of catalysis.

Synthesis of Geometric Isomers of Ru Acetonitrile and Carbonyl Complexes. The Ru precatalyst bearing the NHC *trans* to an acetonitrile ligand, ***C*-Ru-MeCN**$^{2+}$, was prepared according to the previously reported procedure (Scheme 3a).[39] The other geometric isomer, which has not been previously reported, was targeted next. Heating the known "piano stool" complex [(Mebim-py)Ru(*p*-cymene)Cl]-[PF_6][40] with tpy at 80 °C in acetonitrile for 24 h (Scheme 3b) produced a new Ru complex that could be isolated in analytically pure form in 56% yield by column chromatography. The ^{1}H NMR spectrum is consistent with a complex with the formula [Ru(tpy)(Mebim-py)(MeCN)]$^{2+}$ (***N*-Ru-MeCN**$^{2+}$). The signal corresponding to the methyl protons shifted downfield by 1.56 ppm with respect to the analogous signal in ***C*-Ru-MeCN**$^{2+}$, consistent with an *N-trans* isomer in which the methyl protons point away from the terpyridine ring current. ^{13}C NMR spectroscopy revealed a resonance

DOI: 10.1021/jacs.9b01735
J. Am. Chem. Soc. 2019, 141, 6658−6671

Scheme 3. Synthesis of *C*-Ru-MeCN^{2+} (a) and *N*-Ru-MeCN^{2+} (b)

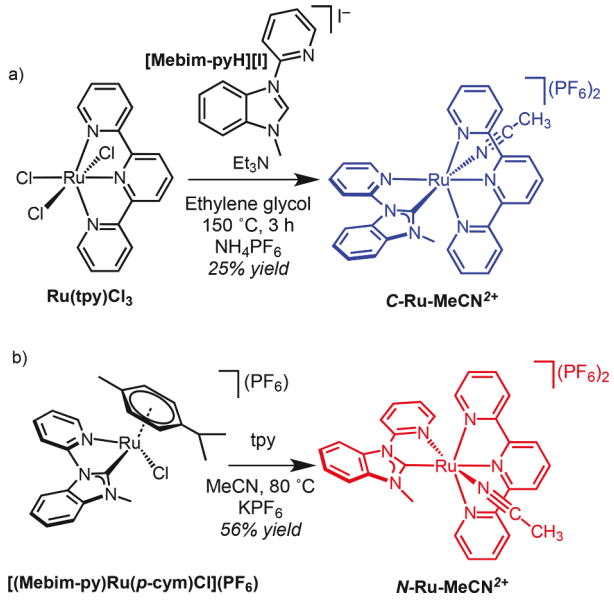

corresponding to the carbene carbon at 210.4 ppm, downfield of the analogous signal in ***C*-Ru-MeCN^{2+}** (203.1 ppm).

Single crystals of ***N*-Ru-MeCN^{2+}** were obtained from an acetone solution layered with pentane. An X-ray diffraction study unambiguously confirmed the connectivity and geometry of the nitrile complex, with the bidentate pyridyl-carbene ligand positioned with the nitrogen atom of the pyridyl group *trans* to the acetonitrile ligand (Figure 4).

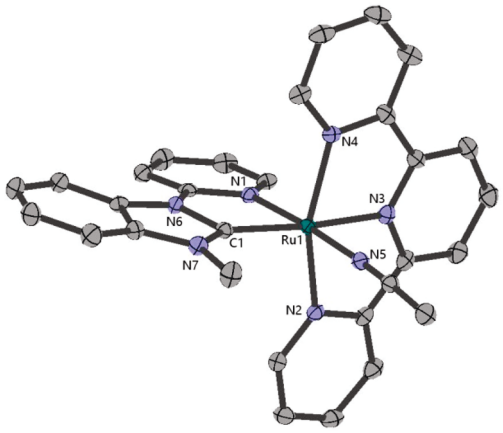

Figure 4. Structural representation of ***N*-Ru-MeCN^{2+}** with ellipsoids drawn at the 50% level. Hydrogen atoms, two PF_6 counterions, and acetone solvent are omitted for clarity. Selected distances (Å) and angles (deg): Ru(1)−C(1) 2.007(3), Ru(1)−N(1) 2.059(2), Ru(1)−N(2) 2.082(2), Ru(1)−N(3) 2.022(2), Ru(1)−N(4) 2.086(2), Ru(1)−N(5) 2.037(2); C(1)−Ru(1)−N(3) 172.32(10), N(5)−Ru(1)−N(1) 175.96(9) N(2)−Ru(1)−N(4) 157.00(9).

Both isomers are stable in CD_3CN solution at room temperature over a period of weeks. After 7 days at 100 °C, solutions of ***C*-Ru-MeCN^{2+}** underwent approximately 10% isomerization to ***N*-Ru-MeCN^{2+}** (see Figure S13 in the SI). Solutions of ***N*-Ru-MeCN^{2+}** underwent 40% isomerization to ***C*-Ru-MeCN^{2+}** under the same conditions (see Figure S14 in the SI). These results are consistent with the DFT predictions that ***C*-Ru-MeCN^{2+}** is thermodynamically more stable, but only by 1−2 kcal/mol.

Metal carbonyl complexes are essential intermediates in electrocatalytic CO production, so the two Ru(II) carbonyl isomers were also targeted. Access to the desired complexes required two distinct synthetic approaches. The *C-trans* isomer was accessed in 53% yield by heating ***C*-Ru-MeCN^{2+}** under 1 atm of CO in EtOH at 75 °C (Scheme 4a). A similar approach

Scheme 4. Synthesis of *C*-Ru-CO^{2+} (a) and *N*-Ru-CO^{2+} (b)

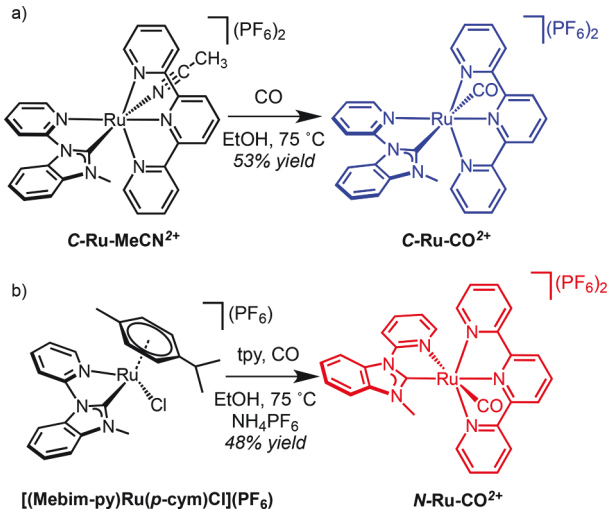

starting from ***N*-Ru-MeCN^{2+}** failed, leading instead to decomposition products and unreacted starting material. An alternative synthesis of ***N*-Ru-CO^{2+}** was developed based on the reaction of [(Mebim-py)Ru(*p*-cymene)Cl][PF_6] with tpy and [NH_4][PF_6] under 1 atm of CO in EtOH at 75 °C (Scheme 4b). A yellow precipitate of ***N*-Ru-CO^{2+}** formed during the course of the reaction, allowing its facile isolation in 48% yield.

The ^{1}H NMR spectra of both complexes are consistent with C_s symmetric structures. The diagnostic signals for the methyl protons appear at 4.56 ppm for ***N*-Ru-CO^{2+}** and at 2.86 ppm for ***C*-Ru-CO^{2+}**. The 1.7 ppm difference provides further evidence that the *N*-methyl proton chemical shift nicely reflects the molecular geometry based on anisotropic effects.[41] The signal attributed to the carbene carbon of ***N*-Ru-CO^{2+}** (203.4 ppm) is shifted downfield compared to ***C*-Ru-CO^{2+}** (195.3 ppm). The resonances corresponding to the carbon of the CO ligand lie at similar chemical shifts (196.0 and 195.3 ppm for ***N*-Ru-CO^{2+}** and ***C*-Ru-CO^{2+}**, respectively). The IR stretching frequencies showed a striking difference of 21 cm^{-1} (ν(CO) = 2026 cm^{-1} for ***C*-Ru-CO^{2+}**, ν(CO) = 2005 cm^{-1} for ***N*-Ru-CO^{2+}** in acetonitrile).

Single-crystal X-ray diffraction of ***C*-Ru-CO^{2+}** and ***N*-Ru-CO^{2+}** reveals overall molecular structures differing only in the relative orientation of the Mebim-py ligand (Figure 5). As expected based on *trans* influence considerations, the Ru−CO distance is longer when positioned *trans* to the carbene ligand (1.960(4) Å in ***C*-Ru-CO^{2+}**) than when positioned *trans* to the pyridine ligand (1.877(4) Å in ***N*-Ru-CO^{2+}**). The carbonyl C−O distance is longer in ***N*-Ru-CO^{2+}** (1.139(5) Å) than in ***C*-Ru-CO^{2+}** (1.124(5) Å), consistent with more π-backbonding into the carbonyl for the *N-trans* complex, in agreement with IR spectroscopy. The carbene is proposed to reduce back-bonding in the M−L unit *trans* to it: in ***C*-Ru-CO^{2+}**, the

DOI: 10.1021/jacs.9b01735
J. Am. Chem. Soc. 2019, 141, 6658−6671

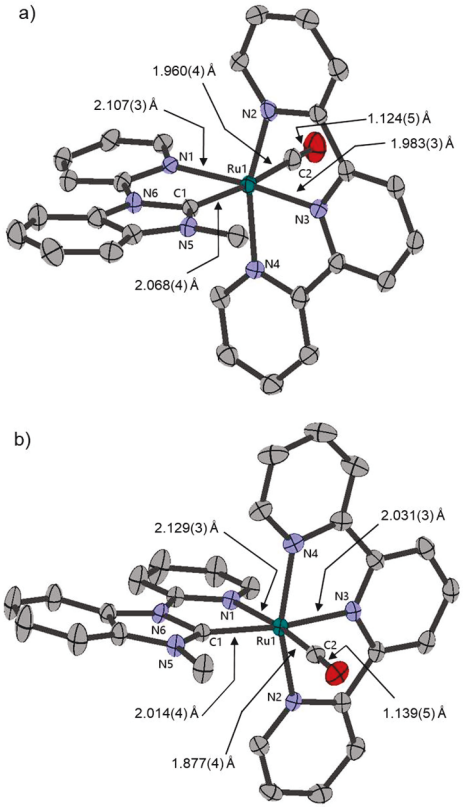

Figure 5. Structural representation of ***C*-Ru-CO**$^{2+}$ (a) and ***N*-Ru-CO**$^{2+}$ (b) with ellipsoids drawn at the 50% level. Hydrogen atoms, two PF_6 for ***C*-Ru-CO**$^{2+}$, two OTf for ***N*-Ru-CO**$^{2+}$ counterions, and acetone solvent are omitted for clarity. See SI for full details on the metrical parameters.

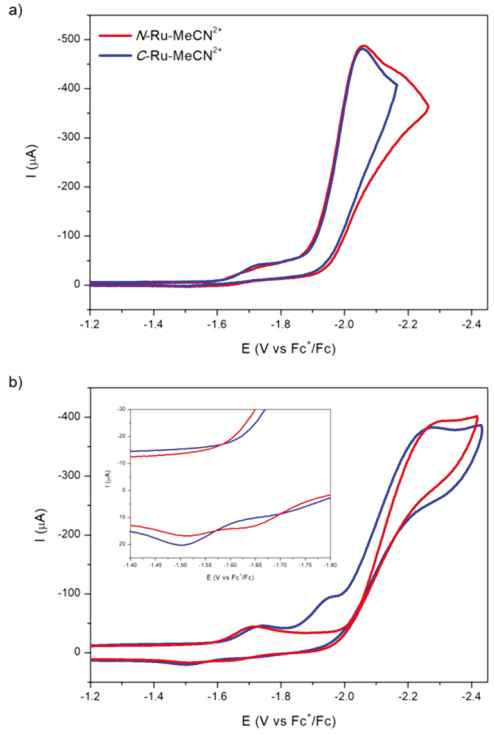

Figure 6. CVs of ***C*-Ru-MeCN**$^{2+}$ (blue) and ***N*-Ru-MeCN**$^{2+}$ (red) at 100 mV/s with a 3 mm working electrode (a) and at 20 V/s with a 1 mm working electrode (b). Inset: Enlargement to show return oxidation features. Conditions: MeCN + 5% H_2O, CO_2 atmosphere, [Ru] = 1 mM, [$TBAPF_6$] = 100 mM, glassy carbon disc working electrode, Pt wire counter electrode, Ag wire pseudoreference electrode.

elongated Ru−CO bond reduces the ability of the CO ligand to accept π electron density. The stretching frequency of the CO ligand in ***N*-Ru-CO**$^{2+}$ is lower because this complex contains a stronger σ-bond with CO and features less π-back-bonding into the tpy ligand, which conspire to maximize π-back-bonding between Ru and CO.

Electrocatalytic CO_2 Reduction by Acetonitrile Complexes. The preliminary studies of the *C-trans* isomer ***C*-Ru-MeCN**$^{2+}$ demonstrated well-behaved cyclic voltammograms (CVs) and selective generation of CO in acetonitrile,[20,26] so this solvent was utilized in our detailed mechanistic analysis of this complex and the newly isolated *N-trans* isomer ***N*-Ru-MeCN**$^{2+}$. The electrocatalytic behavior of each precatalyst isomer was examined to compare overall performance and confirm that the reaction proceeds in a well-defined manner.

CVs of ***C*-Ru-MeCN**$^{2+}$ in dry acetonitrile with no added proton donor under CO_2 show a huge current enhancement near the second reduction feature, indicative of electrocatalytic CO_2 reduction (Figure S17). Electroreduction of CO_2 in the presence of water as a proton source also leads to a strong electrocatalytic response (Figure 6a), in accord with the prior study of this isomer.[26]

The electrocatalytic behavior of ***N*-Ru-MeCN**$^{2+}$ had not been examined previously. Under conditions of dry acetonitrile (Figure S17) as well as 95/5 CH_3CN/H_2O (Figure 6a, 100 mV/s) the precatalyst ***N*-Ru-MeCN**$^{2+}$ exhibits current enhancement that is almost identical to that of ***C*-Ru-MeCN**$^{2+}$.

The water-containing acetonitrile mixtures were the focus of further mechanistic studies, based on the well-defined thermodynamic parameters in this mixed solvent.[42,43] We sought to explore fast-scan-rate conditions for these systems for the first time to enable rate constant analyses, based on the hypothesis that the peak-shaped current responses were due to the catalyst rapidly consuming CO_2 (initial concentration ~0.28 M).[44] Under the conditions outlined above (1 atm CO_2, 95/5 $MeCN/H_2O$), more idealized "S-shaped" peaks could be obtained for both ***C*-Ru-MeCN**$^{2+}$ and ***N*-Ru-MeCN**$^{2+}$ by increasing the CV scan rate above 20 V/s (Figure 6b). This behavior is indicative of kinetically controlled catalysis, wherein the current response is not perturbed by diffusion or substrate consumption.[45,46] As expected for a pure kinetic regime, the peak catalytic current did not vary with scan rate above 20 V/s (Figures S18 and S19 in SI). Under these high scan rate conditions k_{obs}, the rate constant for the rate-determining chemical step in the catalytic cycle, can be estimated using eq 1, which relates the ratio of catalytic current under pure kinetic conditions (i_c) and current in the absence of catalysis (i_p) to k_{obs}, the scan rate (υ), the number of electrons in the overall reaction ($n_c = 2$), and the number of electrons involved in the reduction process in the absence of catalysis ($n_p = 1$).[46,47]

$$\frac{i_c}{i_p} = 2.24\frac{n_c}{n_p}\sqrt{\frac{RT}{n_pF}\sqrt{\frac{1}{\upsilon}}}\sqrt{k_{obs}} \quad (1)$$

The catalytic activity of ***C*-Ru-MeCN**$^{2+}$ (k_{obs} = 2400 ± 200 s^{-1}) is slightly higher that of ***N*-Ru-MeCN**$^{2+}$ (2100 ± 300 s^{-1}), but both precatalysts result in similarly exceptional performance in terms of catalytic activity. A catalytic Tafel plot for the *C-trans* isomer is shown in Figure 7, based on the estimated

DOI: 10.1021/jacs.9b01735
J. Am. Chem. Soc. 2019, 141, 6658−6671

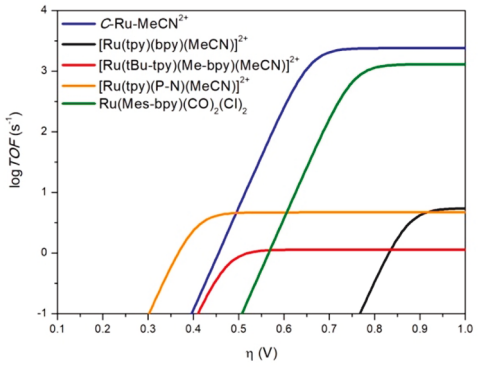

Figure 7. Catalytic Tafel plot of ***C*-Ru-MeCN^{2+}**, plotted alongside other molecular Ru catalysts with well-defined turnover frequency (TOF) and overpotential (η) values. See Section 5 in the SI for structure drawings of [Ru(tpy)(bpy)(MeCN)]$^{2+}$,[20] [Ru(tBu-bpy)-(Me-bpy)(MeCN)]$^{2+}$,[23] [Ru(tpy)(P-N)(MeCN)]$^{2+}$,[31] and Ru(Mes-bpy)(CO)$_2$(Cl)$_2$.[27]

standard potential for the reduction of CO_2 to CO, $E° = -1.44$ V vs Fc^+/Fc,[43] under the employed conditions of 95/5 MeCN/H_2O. The Tafel plot enables comparisons with other Ru electrocatalysts that operate under analogous conditions (see Section 5 in the SI for details related with the construction of the Tafel plots).[20,23] The overpotential required for ***C*-Ru-MeCN^{2+}** to reach a rate constant of 1 s^{-1} is around 450 mV, while the maximum activity is reached at an overpotential around 650 mV.

The precatalyst ***C*-Ru-MeCN^{2+}** features a second reduction before the catalytic wave that is only observed at fast scan rates (Figure 6b). Normalized scan-rate-dependent CVs of ***C*-Ru-MeCN^{2+}** (Figure S20 in the SI) show no substrate consumption in this region, suggesting that no catalysis occurs at the second reduction. Instead, a third reduction is needed to activate ***C*-Ru-MeCN^{2+}** for rapid CO_2 reduction catalysis (the catalytic current enhancement stemming from the third reduction obscures the second reduction at slow scan rates). The catalytic onset thus occurs *just after* the second reduction feature, so a previously unrecognized catalytic intermediate must be undergoing reduction to initiate rapid catalysis. This behavior is consistent with a "reduction first" mechanism[30] involving electrochemical reduction of a metallocarboxylic acid intermediate (pathway A in Scheme 1).

At fast scan rates, CVs of ***N*-Ru-MeCN^{2+}** are distinct from the *C-trans* precatalyst (Figure 6b). The onset of electrocatalysis is observed after only one reduction. While this could reasonably be attributed to the *N-trans* isomer operating via a "protonation first" mechanism (pathway B in Scheme 2), the line crossing observed in CVs of ***N*-Ru-MeCN^{2+}** (Figure 6b) indicates the presence of other chemical processes during the electrochemical experiment.[30] As will be discussed below, the voltammetry of ***N*-Ru-MeCN^{2+}** at all scan rates is consistent with rapid isomerization of an *N-trans* intermediate to a *C-trans* intermediate to produce the same active species regardless of which precatalyst is utilized.

For pathway A, a small primary kinetic isotope effect might be expected. CVs of ***C*-Ru-MeCN^{2+}** under CO_2 in the presence of 5% D_2O reached a higher catalytic peak current than those in the presence of H_2O at 100 mV/s (Figure S21). At first glance, this would suggest an inverse isotope effect, but scan-rate-dependent experiments show that this actually arises from faster substrate depletion kinetics at the surface of the electrode with H_2O. Increasing the scan rate to reach the pure kinetic regime in the presence of D_2O gives $k_{obs} = 1700$ s^{-1} (see Figures S22 and S23 in the SI) and leads to a normal kinetic isotope effect, $k_{obs,H}/k_{obs,D} = 1.4 \pm 0.2$. The small isotope effect is consistent with a rate-determining process that involves either proton transfer to the reduced metallocarboxylic acid or a composite barrier involving pre-equilibrium proton transfer followed by C−O bond cleavage. Similar KIEs have been observed for other CO_2 reduction electrocatalysts proposed to proceed via analogous mechanisms.[48−50]

Controlled potential electrolyses (CPEs) at an applied potential of −2.15 V vs Fc^+/Fc confirm that both catalysts produce CO selectively (Scheme 5), a prerequisite for detailed

Scheme 5. Electrolysis Conditions and Catalytic Performance of the Two Isomeric Precatalysts

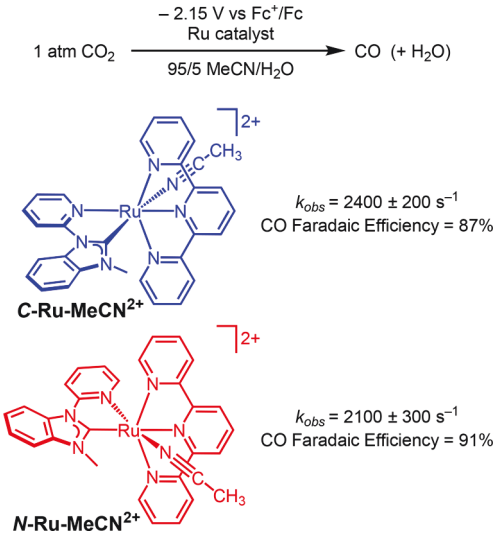

mechanistic studies. Both *C-trans* and *N-trans* isomers supported prolonged current enhancement, although the *C-trans* complex passed somewhat more charge (4.0 C for ***C*-Ru-MeCN^{2+}** and 3.4 C for ***N*-Ru-MeCN^{2+}** during 1 h on a 3 mm glassy carbon disc, Figures S24 and S25 in SI). CO is produced with high Faradaic efficiency by both complexes (87% for ***C*-Ru-MeCN^{2+}** and 91% for ***N*-Ru-MeCN^{2+}**). When reticulated vitreous carbon (RVC) was used as working electrode to increase the area of contact with the solution, a turnover number (TON) of 30 was observed after 1 h based on bulk Ru concentration (much of which is far from the electrode surface and thus inactive at any given time). Accounting for the fraction of catalysts present in the reaction-diffusion layer in CPEs using the glassy carbon disc provides TON values around 10 000 and turnover frequency (TOF) values above 3000 s^{-1}, consistent with the high activity apparent in CVs (see SI Section 3.4 for details). Longer-term CPEs eventually led to a loss of current after approximately 3 h that is attributed to surface adsorption, either of a molecular species that prevents facile electron transfer or by another catalytically inactive species. Polishing the electrode and returning it to the solution resulted in resumed electrocatalysis. Consistent with the low Faradaic efficiency for H_2, electrolysis in 95/5 MeCN/H_2O under N_2 (in the absence of CO_2) led to only traces of hydrogen detected by gas chromatography (GC).

Cyclic Voltammetry Analysis of Initial Reduction: Reduction-Induced Isomerization. To examine the mech-

DOI: 10.1021/jacs.9b01735
J. Am. Chem. Soc. 2019, 141, 6658−6671

anism of electrocatalytic CO production in more detail, a series of cyclic voltammetry studies was carried out to probe the individual mechanistic steps. The initial reduction processes of the two acetonitrile complex isomers were examined first. CVs of ***C*-Ru-MeCN^{2+}** and ***N*-Ru-MeCN^{2+}** in MeCN under an N_2 atmosphere are shown in Figure 8. The current responses of

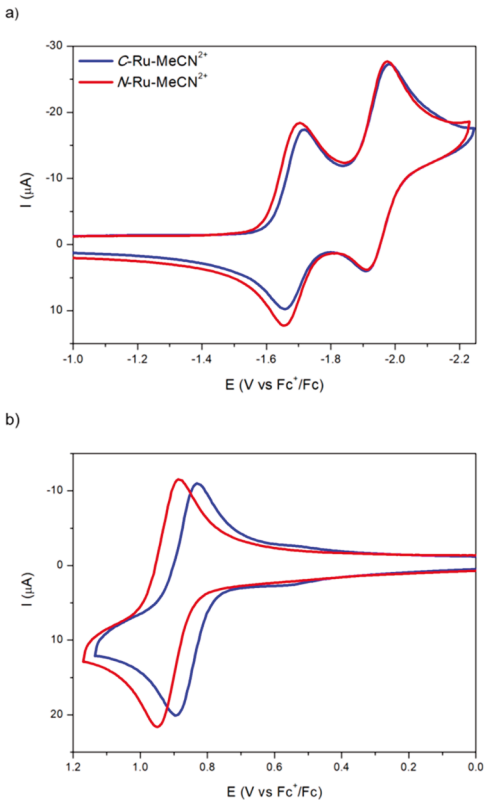

Figure 8. CVs of ***C*-Ru-MeCN^{2+}** (blue) and ***N*-Ru-MeCN^{2+}** (red) showing the cathodic (a) and anodic (b) sections. Conditions: N_2 atmosphere, MeCN, [Ru] = 1 mM, [$TBAPF_6$] = 100 mM, 3 mm glassy carbon disc working electrode, Pt wire counter electrode, Ag wire pseudoreference electrode, 100 mV/s.

the two isomers are nearly indistinguishable, with each complex exhibiting two reversible one-electron reductions (−1.69 and −1.94 V vs Fc^+/Fc for ***C*-Ru-MeCN^{2+}** and −1.68 and −1.94 V vs Fc^+/Fc for ***N*-Ru-MeCN^{2+}**, at 100 mV/s).

CVs of ***N*-Ru-MeCN^{2+}** and ***C*-Ru-MeCN^{2+}** that start with an anodic sweep to positive potentials reveal distinct oxidation features for each complex (Figure 8b). The Ru^{III}/Ru^{II} couple for ***C*-Ru-MeCN^{2+}** (0.86 V vs Fc^+/Fc) is found at less positive potentials than that of ***N*-Ru-MeCN^{2+}** (0.92 V vs Fc^+/Fc). This difference of 60 mV between the oxidation of the two isomers provides a convenient handle to interrogate the identity of the complexes after the two-electron reduction: reduction-induced isomerization of ***N*-Ru-MeCN^{2+}** to the *C-trans* manifold would lead to the appearance of an oxidation at 0.86 V belonging to ***C*-Ru-MeCN^{2+}**.

A series of CVs of ***N*-Ru-MeCN^{2+}** and ***C*-Ru-MeCN^{2+}** were recorded with a full potential sweep at 1 V/s, a scan rate chosen to minimize diffusion of any isomerization products away from the surface of the electrode. CVs of ***C*-Ru-MeCN^{2+}** are exactly the same independently of whether the experiment initially sweeps anodically or cathodically (Figure 9a), indicating that no isomerization occurs for this complex. For

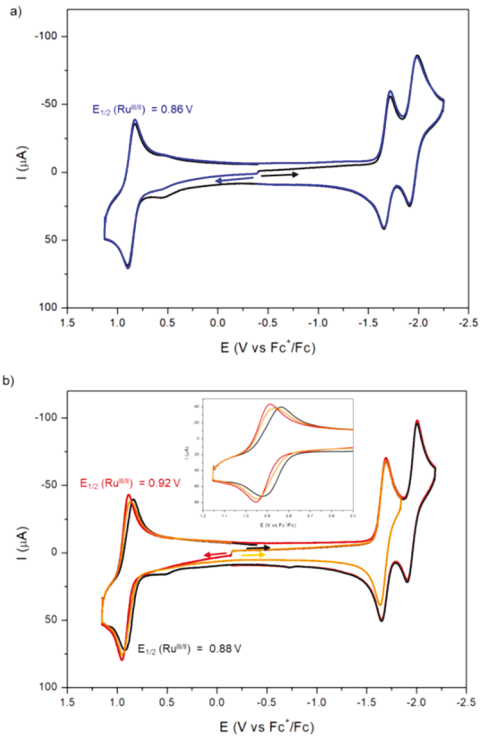

Figure 9. (a) CV of ***C*-Ru-MeCN^{2+}** sweeping anodically (blue) and cathodically (black); (b) CV of ***N*-Ru-MeCN^{2+}** sweeping anodically (red) and cathodically (black and orange). Inset: Zoomed-in oxidation zone. Conditions: N_2 atmosphere, MeCN, [Ru] = 1 mM, [$TBAPF_6$] = 100 mM, 3 mm glassy carbon disc working electrode, Pt wire counter electrode, Ag wire pseudoreference electrode, 1 V/s.

***N*-Ru-MeCN^{2+}**, the half-wave potential of the oxidation feature is different when scanning anodically or cathodically (Figure 9b). After a cathodic sweep through both reduction features, the oxidation feature in the return sweep was observed at $E_{1/2}$ = 0.88 V vs Fc^+/Fc. The oxidation feature agrees closely with that of ***C*-Ru-MeCN^{2+}**, providing clear evidence for *N-trans* to *C-trans* isomerization upon reduction. No change in the oxidation feature of ***N*-Ru-MeCN^{2+}** was observed if the scan was reversed after only the first reduction event, indicating that *two reductions are required to trigger isomerization on this time scale* (Scheme 6). This result is in excellent agreement with our computational study (*vide supra*), in which no minimum could be found for the formally Ru(0) complex with the pyridyl group *trans* to the coordination vacancy. Similar reductive isomerization behavior was observed recently for Ru-tpy-based complexes bearing an asymmetric bidentate P−N ligand.[51] In situ isomerization has also been implicated in photochemical CO_2 reduction by Ir polypyridyl catalysts.[52]

The reduction-induced isomerization process was further probed through a full scan rate dependence of ***N*-Ru-MeCN^{2+}**. At slow scan rates, the second reduction of ***N*-Ru-MeCN^{2+}** (E_{pc2}) appears at the same potential as that of ***C*-Ru-MeCN^{2+}**. The peak potential E_{pc2} of ***N*-Ru-MeCN^{2+}** exhibits a cathodic shift with increasing scan rate (E_{pc2} < −2.1 V vs Fc^+/Fc above 10 V/s Figures S27 and S28 in the SI), which is symptomatic of a chemical step following reduction (EC mechanism).[45] The second reduction remains electrochemically irreversible even at fast scan rates. The anodic return sweep is consistent with oxidation of ***C*-Ru^0** rather than ***N*-Ru^0** at all scan rates, suggesting rapid (≫1000 s^{-1} see Figure S29 in the SI)

DOI: 10.1021/jacs.9b01735
J. Am. Chem. Soc. 2019, 141, 6658−6671

Scheme 6. Electrochemical Reductive Pathways of *C*-Ru-MeCN^{2+} and *N*-Ru-MeCN^{2+} under N_2 (All Potentials *vs* Fc^+/Fc)

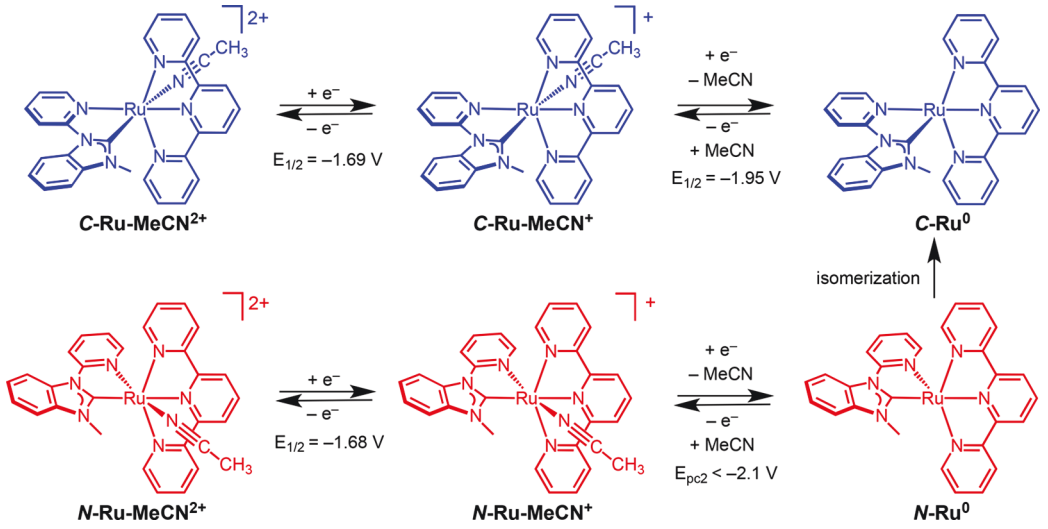

dissociation of MeCN and isomerization to form the more stable five-coordinate species ***C*-Ru^0**.

The cathodic shift of the second reduction of ***N*-Ru-MeCN^{2+}** helps explain why this precatalyst exhibits an unusual catalytic current response at fast scan rates (line crossing and delayed onset, Figure 6b). The onset of catalysis by ***N*-Ru-MeCN^{2+}** is tied to the scan-rate-dependent potential of the second reduction, which triggers acetonitrile dissociation and rapid isomerization to the *C-trans* isomer before binding CO_2. At slow scan rates, nitrile dissociation and isomerization occur on the time scale of the sweep, leading to identical current response for the *N-trans* and *C-trans* isomers (Figure 6a). At fast scan rates, however, the ***N*-Ru-MeCN$^{+/0}$** reduction shifts cathodically beyond −2.1 V vs Fc^+/Fc, while the *C-trans* analogue does not change, resulting in a more negative onset of catalysis for the *N-trans* isomer. After isomerization, the current response increases rapidly and then overlays with that of the *C-trans* species during the return sweep (because the *C-trans* isomer is the dominant species). These observations show that ***N*-Ru-MeCN^{2+}** follows the same mechanism as the *C-trans* isomer (after an initial isomerization) and also helps to explain the line crossover observed at fast scan rates for ***N*-Ru-MeCN^{2+}**.

Reactivity of the Doubly Reduced Intermediate. Initial reduction of either isomer is expected to produce a highly reactive five-coordinate intermediate.[53−55] CV studies are consistent with rapid CO_2 binding and protonation by water to produce a metallocarboxylic acid intermediate. These steps are too rapid for direct electrochemical kinetic studies. In dry MeCN, CO production is attributed to CO_2 binding to form a metallocarboxylate that undergoes nucleophilic attack at a CO_2 molecule to produce CO_3^{2-} as a co-product.[20] Such a change in mechanism is consistent with the 2-fold difference in catalytic current comparing 95/5 MeCN/H_2O and dry MeCN (compare Figure 6a with Figure S17 in the SI).

The five-coordinate doubly reduced intermediate ***C*-Ru^0** could also react with H_2O to form a ruthenium hydride complex. In addition to opening pathways to H_2 or formate, metal hydrides have recently been implicated as intermediates in an alternative mechanism for CO generation (Scheme 1, pathway C).[27] To explore the possibility of Ru protonation by H_2O, separate CVs were obtained for ***C*-Ru-MeCN^{2+}** and ***N*-Ru-MeCN^{2+}** in 95/5 MeCN/H_2O under a N_2 atmosphere (Figures S30 and S31 in the SI). For each isomer, the voltammetric response was almost identical to that in dry MeCN, suggesting that water is not acidic enough to form a metal hydride under these conditions. Thermodynamic calculations based on empirical relationships between reduction potentials and metal hydride pK_a values[56] predict that the hydrides of the two isomers have a lower pK_a than H_2O in MeCN (see SI Section 6). Furthermore, the lack of current enhancement under N_2 suggests that the Ru complexes are not active catalysts for H_2 evolution under these conditions, as corroborated by CPE experiments in the previous section. Further evidence against pathway C of Scheme 1 comes from NMR experiments, which show that ***C*-Ru-MeCN^{2+}** does not produce any CO in the presence of formate. Only H_2 and CO_2 were detected by headspace GC analysis. No evidence for Ru carbonyl species was present by IR spectroscopy or CV studies of ***C*-Ru-MeCN^{2+}** in the presence of formate and H_2O (Figure S32 in SI).

While no evidence is observed for hydride formation in 95/5 MeCN/H_2O, $[Ru(tpy)(Mebim\text{-}py)(OH_2)]^{2+}$ produces H_2/CO mixtures in CO_2-saturated aqueous solutions. Under these conditions near neutral pH values, protonation to form a hydride is the likely pathway to H_2 production. The competing pathways under these conditions were explored computationally, as detailed in the Supporting Information (Section 8).

Electrochemical Studies of CO Complexes: *Trans* Effect on CO Release Rates. After CO_2 binding and activation to form a Ru carbonyl complex, the final step in the catalytic cycle is CO release. With isolated carbonyl complexes in hand, voltammetric studies were conducted to provide insight into the CO release rates for each isomer.

The CV of ***N*-Ru-CO^{2+}** under N_2 in pure MeCN (red trace in Figure 10a) shows two quasi-reversible reductions, both anodically shifted relative to the analogous acetonitrile complex (Figure S33). The first reduction becomes fully reversible ($E_{1/2}$ = −1.44 V vs Fc^+/Fc) if the CV sweep is reversed before reaching the second reduction (Figure S34), consistent with CO dissociation occurring after the second reduction event. The second reduction is quasi-reversible at slow scan rates, but becomes essentially reversible above 6 V/s ($E_{1/2}$ = −1.91 V vs Fc^+/Fc, Figures 10b and S35−S37 in the

DOI: 10.1021/jacs.9b01735
J. Am. Chem. Soc. 2019, 141, 6658−6671

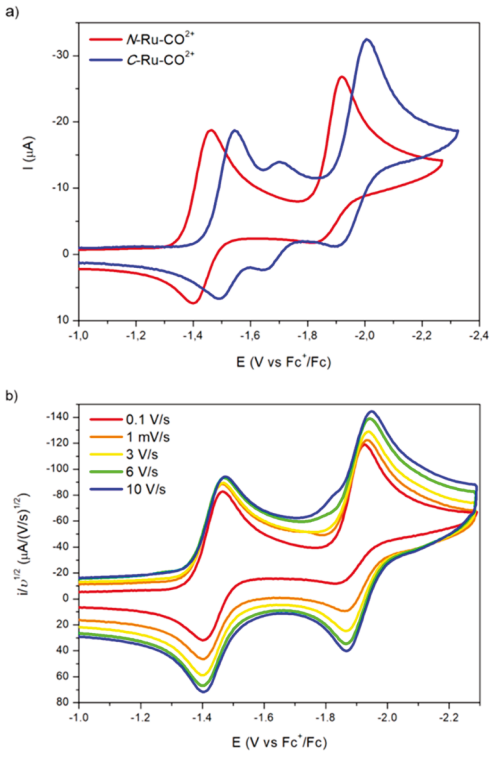

Figure 10. CVs of ***C*-Ru-CO**$^{2+}$ (blue) and ***N*-Ru-CO**$^{2+}$ (red) under N_2 at 100 mV/s scan rate (a) and normalized CVs of ***N*-Ru-CO**$^{2+}$ at various scan rates (b). Conditions: N_2 atmosphere, MeCN, [Ru] = 1 mM, [$TBAPF_6$] = 100 mM, 3 mm glassy carbon disc working electrode, Pt wire counter electrode, Ag wire pseudoreference electrode.

SI). For this type of EC mechanism (Scheme 7) the rate constant for the chemical step can be estimated according to a zone diagram analysis based on the scan rate (υ) at which the reaction becomes fully reversible, $k_{CO} \leq 6\upsilon$.[45] The rate constant for CO dissociation was estimated to be $k_{CO} \leq 36\ s^{-1}$.

The rate constant for CO dissociation upon 2e$^-$ *reduction of* ***N*-Ru-CO**$^{2+}$ *is more than 50 times slower than the observed rate constant for electrochemical catalysis starting from* ***N*-Ru-MeCN**$^{2+}$, *clearly ruling out the N-trans Ru carbonyl complex as a competent catalytic intermediate.*

The CV of ***C*-Ru-CO**$^{2+}$ under N_2 features two major reductions that are cathodically shifted relative to ***N*-Ru-CO**$^{2+}$ (Figure 10a blue trace). A less prominent, reversible reduction ($E_{1/2} = -1.69$ V vs Fc^+/Fc) is observed at the same potential as the first reduction of ***C*-Ru-MeCN**$^{2+}$ (Figure S38). NMR spectroscopic monitoring of ***C*-Ru-CO**$^{2+}$ in CD_3CN (Figures S7 and S15a) confirms partial CO substitution by the solvent over several minutes. Heating ***C*-Ru-CO**$^{2+}$ for 3 h at 100 °C gives full conversion to ***C*-Ru-MeCN**$^{2+}$ (in contrast, ***N*-Ru-CO**$^{2+}$ does not lose CO or isomerize after 1 week at 100 °C; see Figures S15 and S16 in the SI).

The CV of ***C*-Ru-CO**$^{2+}$ provides insight into catalytic intermediates. An anodic feature (approximately −1.5 V vs Fc^+/Fc) present in the return sweeps of electrocatalytic CV experiments (Figure 6b) aligns perfectly with the *C-trans carbonyl species* (***C*-Ru-CO**$^{2+}$/***C*-Ru-CO**$^{+}$ couple, Figure 10a). The electrocatalytic response of *both* acetonitrile complexes ***C*-Ru-MeCN**$^{2+}$ and ***N*-Ru-MeCN**$^{2+}$ shows the same anodic feature, further confirming that the *N-trans* complex isomerizes to the *C-trans* under catalytic conditions. Following CPE experiments using either ***C*-Ru-NCMe**$^{2+}$ or ***N*-Ru-NCMe**$^{2+}$ precatalyst, CVs match perfectly with ***C*-Ru-CO**$^{2+}$ (Figures S39−S41 in SI). The presence of ***C*-Ru-CO**$^{2+}$ in solution after CPE was further established by IR spectroscopy (Figures S42 and S43, no evidence of ***N*-Ru-CO**$^{2+}$ was observed), confirming full isomerization to *C-trans* species during catalysis starting from ***N*-Ru-MeCN**$^{2+}$.

The distinct reduction potentials of the carbonyl and acetonitrile complexes enable studies of reductively triggered CO displacement by acetonitrile. A CV at 100 mV/s that sweeps cathodically through the one-electron reduction of ***C*-Ru-CO**$^{2+}$ releases CO to generate more ***C*-Ru-MeCN**$^{2+}$, based on the current increase for the oxidation feature attributed to the acetonitrile complex (Figure S44 in SI). CVs of ***C*-Ru-CO**$^{2+}$ at scan rates of 50 and 25 mV/s show a marked increase in peak current for the reduction of ***C*-Ru-MeCN**$^{2+}$ even in the initial cathodic sweep, further indicating CO loss after a single reduction (Figures S46 and S47 in the SI). A chemical disproportionation involving oxidation of ***C*-Ru-MeCN**$^{+}$ by ***C*-Ru-CO**$^{2+}$ could account for the presence of increasing amounts of ***C*-Ru-MeCN**$^{2+}$ in the voltammograms. At faster scan rates (e.g., 1 V/s), there is little evidence for CO loss from ***C*-Ru-CO**$^{+}$ (Figure S45 in the SI).

Sweeping to more negative potentials leads to reduction of ***C*-Ru-CO**$^{+}$ with a voltammetric response that is essentially irreversible. In accord with rapid CO dissociation upon two-electron reduction of ***C*-Ru-CO**$^{2+}$ is the observation of a large increase in the peak current for the features associated with oxidation of ***C*-Ru-MeCN**$^{2+}$, even at a scan rate of 1 V/s (Figure S45 in the SI). The reductions of ***C*-Ru-CO**$^{+}$ and ***C*-Ru-MeCN**$^{+}$ are not easily distinguishable because they occur at almost the same potential. This lends some apparent reversibility to the CV, but this feature is assigned as an irreversible reduction of ***C*-Ru-CO**$^{+}$ due to rapid following CO loss overlapping with the reversible reduction of ***C*-Ru-MeCN**$^{+}$. The presence of ***C*-Ru-MeCN**$^{2+}$ prevents a full kinetic analysis for the CO dissociation upon reduction of ***C*-Ru-CO**$^{+}$, but the scan rate dependence studies are consistent with an extremely rapid process. Scheme 8 shows a reaction sequence that accounts for the observed behavior. *The C-trans carbonyl complex* ***C*-Ru-CO**$^{2+}$ *is a kinetically competent catalytic*

Scheme 7. Electrochemical Reductive Mechanism of *N*-Ru-CO^{2+} under N_2 (All Potentials *vs* Fc^+/Fc)

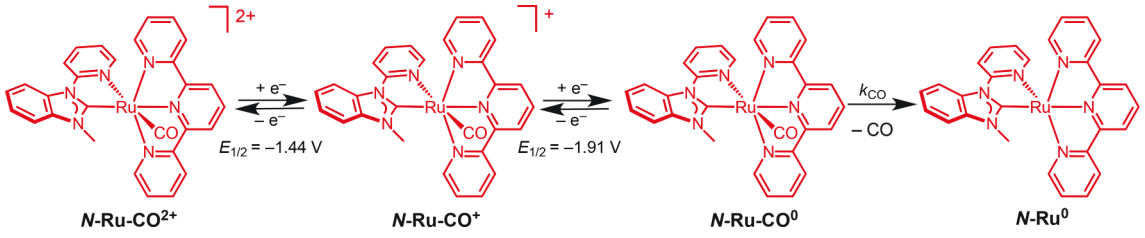

DOI: 10.1021/jacs.9b01735
J. Am. Chem. Soc. 2019, 141, 6658−6671

Scheme 8. Electrochemical Reductive Pathways for *C*-Ru-CO^{2+} under N_2 (All Potentials *vs* Fc$^+$/Fc)

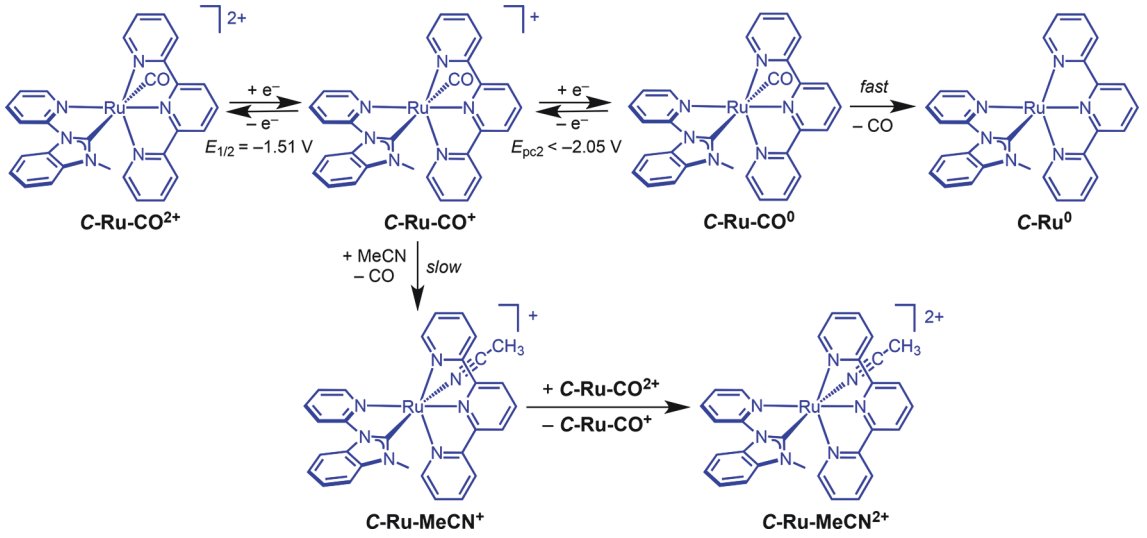

intermediate, whereas the N-trans analogue is not. This suggests that, although ***N*-Ru-CO**$^{2+}$ *is thermodynamically more stable than* ***C*-Ru-CO**$^{2+}$*, it is not formed during catalysis.*

The CO dissociation processes were also monitored using infrared spectroelectrochemistry (IR-SEC). Upon stepwise reduction of ***N*-Ru-CO**$^{2+}$, the CO stretching band assigned to this complex (2005 cm^{-1}) decreases in intensity, while a new band located at 1961 cm^{-1} grows (Figure S48). The new CO stretching band is assigned to the singly reduced complex ***N*-Ru-CO**$^{+}$. Further reduction at more negative potentials leads to the disappearance of all IR signals in the CO stretching region, in agreement with CO loss occurring only after the two-electron reduction of ***N*-Ru-CO**$^{2+}$. When the same experiment was performed with ***C*-Ru-CO**$^{2+}$ (2026 cm^{-1}), the initial vibrational feature decreased in intensity upon single reduction faster than the *N-trans* complex. The resulting band (1975 cm^{-1}), assigned to ***C*-Ru-CO**$^{+}$, was relatively lower in intensity (Figure S49), consistent with some CO dissociation during the first reduction as observed by CV. Full CO loss is observed upon applying more negative potentials, indicating rapid and quantitative CO release after the second reduction.

If a *C-trans* carbonyl complex is a catalytic intermediate, ***C*-Ru-CO**$^{2+}$ should be a viable precatalyst for CO_2 electroreduction. Indeed, CVs of ***C*-Ru-CO**$^{2+}$ in 95/5 MeCN/H_2O under a CO_2 atmosphere show a catalytic wave that looks almost identical to those observed for the nitrile complexes (Figure 11 and Figure S41). Furthermore, increasing the scan rate of the experiment results in plateau-shaped CVs (Figure S50), providing k_{obs} = 2300 s^{-1}; this value is the same within error as the value obtained for ***C*-Ru-MeCN**$^{2+}$.

On the other hand, CVs of ***N*-Ru-CO**$^{2+}$ under the same conditions show only a modest current enhancement at the second reduction feature, with a somewhat larger current response observed at more negative potentials than seen for the acetonitrile complexes (Figure 11). The delayed onset beyond −2 V is attributed to sluggish dissociation, with slow CO release kinetics limiting access to the intermediate that rapidly isomerizes to the *C-trans* manifold. The catalytic rate constant for ***N*-Ru-CO**$^{2+}$ was estimated as described above as k_{obs} = 1600 s^{-1}, much smaller than for the acetonitrile complexes and also requiring higher overpotential. Interestingly, no catalytic activity at all is observed for ***N*-Ru-CO**$^{2+}$ in

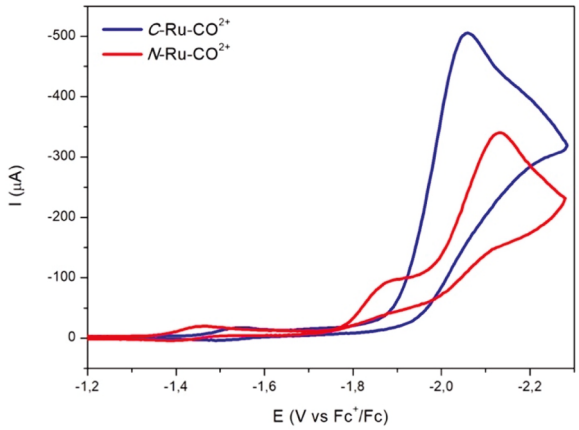

Figure 11. CVs of ***C*-Ru-CO**$^{2+}$ (blue) and ***N*-Ru-CO**$^{2+}$ (red), under CO_2 atmosphere with 5% H_2O. Conditions: CO_2 atmosphere, MeCN + 5% H_2O, [Ru] = 1 mM, [$TBAPF_6$] = 100 mM, 3 mm glassy carbon disc working electrode, Pt wire counter electrode, Ag wire pseudoreference electrode, 100 mV/s.

dry MeCN (Figure S51), suggesting a role of water in accelerating CO dissociation or isomerization.

Mechanistic Summary. The overall mechanistic picture is captured in Scheme 9. The onset of catalysis beyond the second reduction feature of ***C*-Ru-MeCN**$^{2+}$ is consistent with a "reduction first" pathway (pathway A in Scheme 1) that is essentially unknown for Ru catalysts, but common for Mn and Re catalysts.[57] Pathway B is ruled out because the catalytic onset should occur at the second reduction feature, not at more negative potentials as seen in the experiments. Pathway C is ruled out on the basis of an array of studies showing that Ru hydrides are not formed under the reaction conditions and that formate is not an intermediate. Pathway D is ruled out because the first reduction feature is not perturbed by CO_2.

Initial reduction proceeds by sequential one-electron processes, followed by acetonitrile dissociation. In the case of ***N*-Ru-MeCN**$^{2+}$, the second reduction is followed by an isomerization process that is sufficiently rapid (≫1000 s^{-1}) to be kinetically competent in catalysis. After reduction (and isomerization in the case of *N-trans* complexes), rapid CO_2 binding produces *only* the *C-trans* isomer ***C*-Ru-CO**$^{+}$ upon

DOI: 10.1021/jacs.9b01735
J. Am. Chem. Soc. 2019, 141, 6658−6671

Scheme 9. Overall Mechanistic Scheme

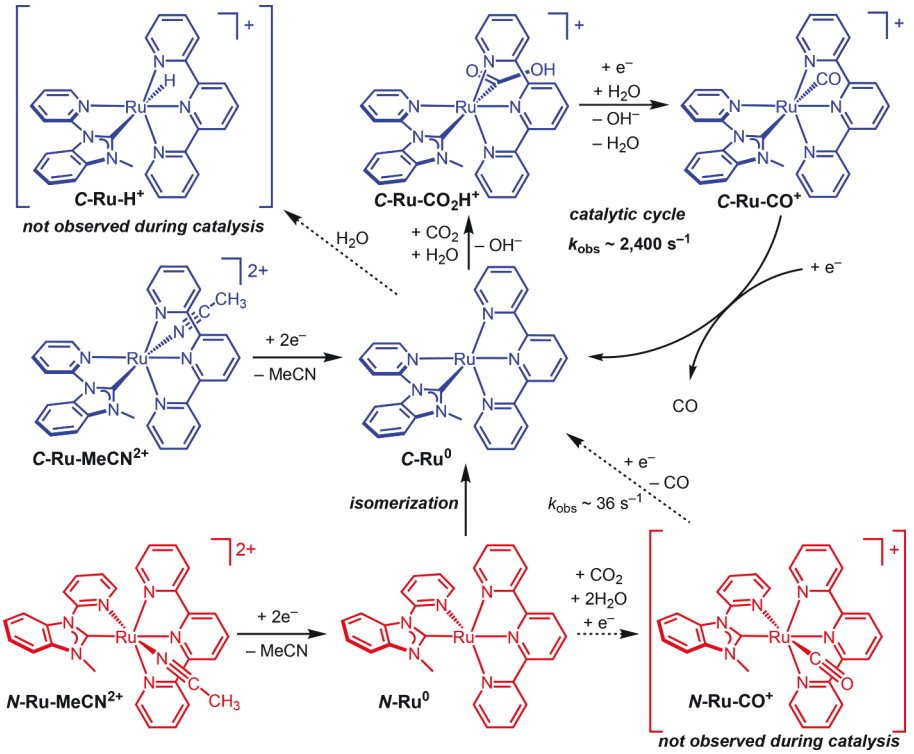

protonation and reduction of the metallocarboxylate. The more thermodynamically stable *N-trans* isomer ***N*-Ru-CO**$^{2+}$ and its reduced analogues are not observed. Reduction of ***N*-Ru-MeCN**$^{2+}$ triggers isomerization to the *C-trans* manifold, proceeding faster than any reactivity with CO_2 that would form an *N-trans* carbonyl complex. There is also a kinetic barrier to isomerization of the carbonyl complexes: once the *C-trans* carbonyl complexes form, they do not isomerize to the *N-trans* isomers. This is fortuitous, because ***N*-Ru-CO**$^{2+}$ undergoes CO dissociation upon reduction at a rate ($k_{CO} \leq 36\ s^{-1}$) that is far too slow to be competent in catalysis. The *trans* effect of the carbene plays a key role in catalysis. With the carbene *trans* to CO, both ***C*-Ru-CO**$^{+}$ and ***C*-Ru-CO**^{0} support extremely facile CO dissociation, consistent with the intermediacy of such species in catalysis.

Connections to Surface Electrocatalysis. A recent report from Meyer and co-workers demonstrated CO production from surface-bound ruthenium pyridyl-carbene complexes that are closely related to the freely diffusing species under examination here.[58] In that work, the *C-trans* Ru complex of Figure 12 was attached to a glass slide sequentially treated with TiO_2, carbon nanotubes, and another layer of TiO_2. After an overcoat of TiO_2 was added to stabilize the catalyst−surface interaction, electrolysis in aqueous $NaHCO_3$ buffer under 1 atm of CO_2 led to CO production with a TON > 300. All of the CO was produced in an initial burst of activity, however; complete catalyst deactivation was observed after just 900 s. Most of the Ru remained on the surface, but high-resolution X-ray photoelectron spectroscopy (XPS) revealed a change in the Ru binding energy before and after electrolysis.

Hypothesizing that the modified electrodes might be deactivating to one of the three new Ru species synthesized in this work, we carried out XPS studies to characterize the Ru binding energy of each of the four isolated complexes. Figure 12 compares the Ru binding energies of the molecular species with the postcatalysis electrode material. An excellent agreement in Ru binding energy is observed for ***N*-Ru-CO**$^{2+}$ (green trace) and the deactivated surface-modified electrode (black trace). The loss in catalytic activity of the molecule-decorated electrode might therefore be due to an isomerization event to form the *N-trans* carbonyl complex that was demonstrated in the present study to have poor catalytic activity. While the origins of this change in mechanism on the surface warrant

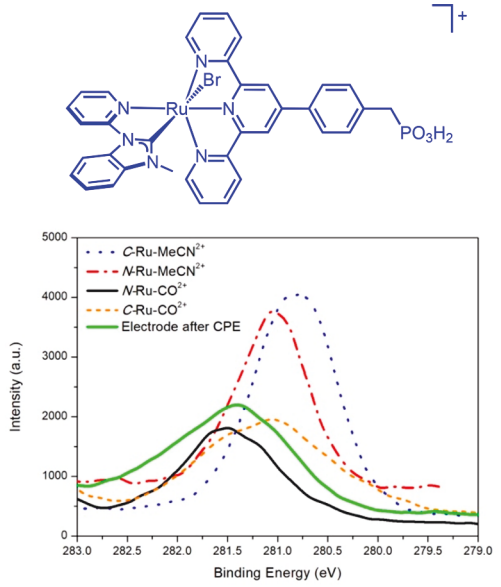

Figure 12. Structure of Ru pyridyl-carbene catalyst studied on surfaces (top) and XPS spectra of the modified electrode after controlled potential electrolysis (CPE) and the various molecular complexes prepared in the present work (bottom).

DOI: 10.1021/jacs.9b01735
J. Am. Chem. Soc. 2019, 141, 6658−6671

further investigation, this observation underscores the importance of controlling catalyst geometry.

CONCLUSIONS

The experimental and computational results paint a detailed portrait of the mechanism of a leading electrocatalyst for CO production. Three key features of the ruthenium terpyridine pyridyl-carbene catalysts stand out as design principles that could be applied to other electrocatalysts: (1) the *trans* effect can accelerate key steps in CO_2 electroreduction, (2) geometric isomerization of the catalyst during turnover can play a pivotal role, and (3) heteroleptic complexes mixing strong donor ligands and redox-active ligands can balance high activity and low overpotential. These three features are discussed in more detail in the following paragraphs.

With the structures of molecular electrocatalysts continually increasing in complexity, it is becoming more important to understand the opportunities and challenges associated with geometric isomers. One key feature of the present system is the *trans* effect revealed by the asymmetric pyridyl-carbene ligand. Positioning the strong N-heterocyclic carbene donor *trans* to the CO_2 activation site enables extremely rapid CO_2 electroreduction (k_{obs} = 2400 s^{-1}). This is reflected in the rates of key steps: for example, the *C-trans* Ru carbonyl complex undergoes CO dissociation much more rapidly than the *N-trans* analogue. This difference in rate does not come at the expense of a more negative reduction potential; in fact, the *C-trans* analogues are more reactive and also easier to reduce. These observations suggest that future catalysts should be designed to position a single strong donor ligand *trans* to the CO_2 activation site.

The *trans* effect is only observed because the stereochemistry of the present catalyst system is kinetically controlled. Although *N-trans* intermediates are thermodynamically favored in the late stages of the catalytic cycle, both *N-trans* and *C-trans* precatalysts proceed via a pathway that kinetically enforces *C-trans* stereochemistry. Initial reduction of ***N*-Ru-MeCN^{2+}** triggers isomerization to *C-trans* isomers, enabling rapid electrocatalysis from either precatalyst. Isomerization at the doubly reduced state "locks in" the molecular geometry, introducing a kinetic barrier to access *N-trans* isomers during the remainder of the catalytic cycle. Significantly, this avoids formation of the carbonyl complex ***N*-Ru-CO^{2+}**, which is more stable than ***C*-Ru-CO^{2+}** but undergoes prohibitively slow CO release. The catalyst system can be considered "self-corrective" because reduction of an *N-trans* isomer funnels the catalyst into the highly active *C-trans* orientation. While the catalysis proceeds in an ideal fashion in solution, the XPS study suggests that a surface-bound variant of the Ru pyridyl-carbene catalyst isomerizes to an inactive *N-trans* carbonyl complex. The notion that geometric isomerization along the catalytic cycle may be a general phenomenon is supported by the observation that *photochemical* CO_2 reduction catalyzed by $[Ir(tpy)(ppy)(Cl)]^+$ (ppy is 2-phenylpyridine) also proceeds through a common five-coordinate intermediate with the strong σ-donor *trans* to the coordination vacancy.[52,59]

Another general design principle is apparent in the pairing of the pyridyl-carbene ligand with the redox-active tpy ligand. The computational and experimental data are consistent with the first and second reductions having a high degree of tpy character. The pyridyl-carbene can therefore tune the nucleophilicity to enhance ligand dissociation and CO_2 activation rates without greatly impacting the reduction potentials. This strategy of decoupling electronic tuning of nucleophilicity and redox potentials is distinct from many catalyst systems. For example, electronic tuning in variants of $Re(bpy)(CO)_3(Cl)$ by adjusting the substituents on the bipyridine ligand leads to scaling relationships in which the fastest catalysts are the hardest to reduce.[30] Similar observations have been made for $[Ru(tpy)(bpy)(L)]^{2+}$ analogues.[21] Tuning the properties of a redox-inactive ligand while maintaining the electronic structure of the redox-active ligand involved in accepting electrons has the potential to break commonly observed scaling relationships.

These new mechanistic insights have enabled a deeper understanding of the underlying features that engender Ru pyridyl-carbene with excellent catalytic activity. These findings have broad implications in catalyst design, highlighting opportunities for precise catalyst control when the appropriate geometric isomers can be harnessed.

ASSOCIATED CONTENT

Supporting Information

The Supporting Information is available free of charge on the ACS Publications website at DOI: 10.1021/jacs.9b01735.

Experimental details, NMR spectra, electrochemical methods, crystallographic methods, and computational methods (PDF)

Crystallographic data (CIF)

Coordinates for optimized geometries in MeCN (PDF)

Coordinates for optimized geometries in H_2O (PDF)

AUTHOR INFORMATION

Corresponding Author

*ajmm@email.unc.edu

ORCID

Sergio Gonell: 0000-0003-0517-6833

Alexander J. M. Miller: 0000-0001-9390-3951

Notes

The authors declare no competing financial interest.

ACKNOWLEDGMENTS

This material is based upon work solely supported as part of the Alliance for Molecular PhotoElectrode Design for Solar Fuels (AMPED), an Energy Frontier Research Center (EFRC) funded by the U.S. Department of Energy, Office of Science, Office of Basic Energy Sciences, under Award Number DE-SC0001011. J.T.M. used computing facilities at Brookhaven National Laboratory (BNL) that were supported by the U.S. Department of Energy, Office of Science, Office of Basic Energy Sciences, under Award Number DE- SC0012704. This work was performed in part at the Chapel Hill Analytical and Nanofabrication Laboratory, CHANL, a member of the North Carolina Research Triangle Nanotechnology Network, RTNN, which is supported by the National Science Foundation, Grant ECCS-1542015, as part of the National Nanotechnology Coordinated Infrastructure, NNCI. Quinton J. Bruch assisted with crystallographic data collection. We thank Brandie M. Ehrmann for assistance at the University of North Carolina at Chapel Hill Department of Chemistry Mass Spectrometry Core Laboratory, in work supported by the National Science Foundation under Grant No. CHE-1726291.

DOI: 10.1021/jacs.9b01735
J. Am. Chem. Soc. 2019, 141, 6658−6671

REFERENCES

(1) Benson, E. E.; Kubiak, C. P.; Sathrum, A. J.; Smieja, J. M. Electrocatalytic and Homogeneous Approaches to Conversion of CO_2 to Liquid Fuels. *Chem. Soc. Rev.* **2009**, *38*, 89−99.

(2) Finn, C.; Schnittger, S.; Yellowlees, L. J.; Love, J. B. Molecular Approaches to the Electrochemical Reduction of Carbon Dioxide. *Chem. Commun.* **2012**, *48*, 1392−1399.

(3) Qiao, J.; Liu, Y.; Hong, F.; Zhang, J. A Review of Catalysts for the Electroreduction of Carbon Dioxide to Produce Low-Carbon Fuels. *Chem. Soc. Rev.* **2014**, *43*, 631−675.

(4) Taheri, A.; Berben, L. A. Making C−H Bonds with CO_2: Production of Formate by Molecular Electrocatalysts. *Chem. Commun.* **2016**, *52*, 1768−1777.

(5) Costentin, C.; Savéant, J.-M. Towards an Intelligent Design of Molecular Electrocatalysts. *Nat. Rev. Chem.* **2017**, *1*, 0087.

(6) Francke, R.; Schille, B.; Roemelt, M. Homogeneously Catalyzed Electroreduction of Carbon Dioxide—Methods, Mechanisms, and Catalysts. *Chem. Rev.* **2018**, *118*, 4631−4701.

(7) Gonell, S.; Miller, A. J. M. Carbon Dioxide Electroreduction Catalyzed by Organometallic Complexes. In *Advances in Organometallic Chemistry*; Elsevier Inc., 2018; Vol. *70*, pp 1−69.

(8) Aresta, M.; Dibenedetto, A. Utilisation of CO_2 as a Chemical Feedstock: Opportunities and Challenges. *Dalt. Trans.* **2007**, *28*, 2975.

(9) Inglis, J. L.; MacLean, B. J.; Pryce, M. T.; Vos, J. G. Electrocatalytic Pathways towards Sustainable Fuel Production from Water and CO_2. *Coord. Chem. Rev.* **2012**, *256*, 2571−2600.

(10) Appel, A. M.; Bercaw, J. E.; Bocarsly, A. B.; Dobbek, H.; DuBois, D. L.; Dupuis, M.; Ferry, J. G.; Fujita, E.; Hille, R.; Kenis, P. J.; et al. Frontiers, Opportunities, and Challenges in Biochemical and Chemical Catalysis of CO_2 Fixation. *Chem. Rev.* **2013**, *113*, 6621−6658.

(11) Takeda, H.; Cometto, C.; Ishitani, O.; Robert, M. Electrons, Photons, Protons and Earth-Abundant Metal Complexes for Molecular Catalysis of CO_2 Reduction. *ACS Catal.* **2017**, *7*, 70−88.

(12) Berardi, S.; Drouet, S.; Francàs, L.; Gimbert-Suriñach, C.; Guttentag, M.; Richmond, C.; Stoll, T.; Llobet, A. Molecular Artificial Photosynthesis. *Chem. Soc. Rev.* **2014**, *43*, 7501−7519.

(13) Kang, P.; Chen, Z.; Brookhart, M.; Meyer, T. J. Electrocatalytic Reduction of Carbon Dioxide: Let the Molecules Do the Work. *Top. Catal.* **2015**, *58*, 30−45.

(14) Elgrishi, N.; Chambers, M. B.; Wang, X.; Fontecave, M. Molecular Polypyridine-Based Metal Complexes as Catalysts for the Reduction of CO_2. *Chem. Soc. Rev.* **2017**, *46*, 761−796.

(15) Ishida, H.; Fujiki, K.; Ohba, T.; Ohkubo, K.; Tanaka, K.; Terada, T.; Tanaka, T. Ligand Effects of Ruthenium 2,2′-Bipyridine and 1,10-Phenanthroline Complexes on the Electrochemical Reduction of CO_2. *J. Chem. Soc., Dalton Trans.* **1990**, *2*, 2155−2160.

(16) Ishida, H.; Tanaka, K.; Tanaka, T. Electrochemical CO_2 Reduction Catalyzed by Ruthenium Complexes $[Ru(bpy)_2(CO)_2]^{2+}$ and $[Ru(bpy)_2(CO)Cl]^{+}$. Effect of pH on the Formation of CO and $HCOO^{-}$. *Organometallics* **1987**, *6*, 181−186.

(17) Collomb-Dunand-Sauthier, M.-N.; Deronzier, A.; Ziessel, R. Electrocatalytic Reduction of Carbon Dioxide with Mono(Bipyridine)Carbonylruthenium Complexes in Solution or as Polymeric Thin Films. *Inorg. Chem.* **1994**, *33*, 2961−2967.

(18) Chardon-Noblat, S.; Collomb-Dunand-Sauthier, M.-N.; Deronzier, A.; Ziessel, R.; Zsoldos, D. Formation of Polymeric $[\{Ru^0(bpy)(CO)_2\}_n]$ Films by Electrochemical Reduction of $[Ru(bpy)_2(CO)_2](PF_6)_2$: Its Implication in CO_2 Electrocatalytic Reduction. *Inorg. Chem.* **1994**, *33*, 4410−4412.

(19) Nagao, H.; Mizukawa, T.; Tanaka, K. Carbon-Carbon Bond Formation in the Electrochemical Reduction of Carbon Dioxide Catalyzed by a Ruthenium Complex. *Inorg. Chem.* **1994**, *33*, 3415−3420.

(20) Chen, Z.; Chen, C.; Weinberg, D. R.; Kang, P.; Concepcion, J. J.; Harrison, D. P.; Brookhart, M. S.; Meyer, T. J. Electrocatalytic Reduction of CO_2 to CO by Polypyridyl Ruthenium Complexes. *Chem. Commun.* **2011**, *47*, 12607−12609.

(21) White, T. A.; Maji, S.; Ott, S. Mechanistic Insights into Electrocatalytic CO_2 Reduction within $[Ru^{II}(tpy)(NN)X]^{n+}$ Architectures. *Dalton Trans* **2014**, *43*, 15028−15037.

(22) Chen, Z.; Kang, P.; Zhang, M.-T.; Meyer, T. J. Making Syngas Electrocatalytically Using a Polypyridyl Ruthenium Catalyst. *Chem. Commun.* **2014**, *50*, 335−337.

(23) Johnson, B. A.; Maji, S.; Agarwala, H.; White, T. A.; Mijangos, E.; Ott, S. Activating a Low Overpotential CO_2 Reduction Mechanism by a Strategic Ligand Modification on a Ruthenium Polypyridyl Catalyst. *Angew. Chem., Int. Ed.* **2016**, *55*, 1825−1829.

(24) Das, B.; Ezzedinloo, L.; Bhadbhade, M.; Bucknall, M. P.; Colbran, S. B. Strategic Design of a Ruthenium Catalyst for Both CO_2 Reduction and H_2O Oxidation: The Electronic Influence of the Co-Ligands. *Chem. Commun.* **2017**, *53*, 10006−10009.

(25) Kang, P.; Chen, Z.; Nayak, A.; Zhang, S.; Meyer, T. J. Single Catalyst Electrocatalytic Reduction of CO_2 in Water to H_2 + CO Syngas Mixtures with Water Oxidation to O_2. *Energy Environ. Sci.* **2014**, *7*, 4007−4012.

(26) Chen, Z.; Concepcion, J. J.; Brennaman, M. K.; Kang, P.; Norris, M. R.; Hoertz, P. G.; Meyer, T. J. Splitting CO_2 into CO and O_2 by a Single Catalyst. *Proc. Natl. Acad. Sci. U. S. A.* **2012**, *109*, 15606−15611.

(27) Machan, C. W.; Sampson, M. D.; Kubiak, C. P. A Molecular Ruthenium Electrocatalyst for the Reduction of Carbon Dioxide to CO and Formate. *J. Am. Chem. Soc.* **2015**, *137*, 8564−8571.

(28) Min, S.; Rasul, S.; Li, H.; Grills, D. C.; Takanabe, K.; Li, L.-J.; Huang, K.-W. Electrocatalytic Reduction of Carbon Dioxide with a Well-Defined PN^3−Ru Pincer Complex. *ChemPlusChem* **2016**, *81*, 166−171.

(29) Sampson, M. D.; Nguyen, A. D.; Grice, K. A.; Moore, C. E.; Rheingold, A. L.; Kubiak, C. P. Manganese Catalysts with Bulky Bipyridine Ligands for the Electrocatalytic Reduction of Carbon Dioxide: Eliminating Dimerization and Altering Catalysis. *J. Am. Chem. Soc.* **2014**, *136*, 5460−5471.

(30) Clark, M. L.; Cheung, P. L.; Lessio, M.; Carter, E. A.; Kubiak, C. P. Kinetic and Mechanistic Effects of Bipyridine (bpy) Substituent, Labile Ligand, and Brønsted Acid on Electrocatalytic CO_2 Reduction by Re(bpy) Complexes. *ACS Catal.* **2018**, *8*, 2021−2029.

(31) Lee, S. K.; Kondo, M.; Nakamura, G.; Okamura, M.; Masaoka, S. Low-Overpotential CO_2 Reduction by a Phosphine-Substituted Ru(II) Polypyridyl Complex. *Chem. Commun.* **2018**, *54*, 6915−6918.

(32) Ramakrishnan, S.; Chidsey, C. E. D. Initiation of the Electrochemical Reduction of CO_2 by a Singly Reduced Ruthenium-(II) Bipyridine Complex. *Inorg. Chem.* **2017**, *56*, 8326−8333.

(33) Frisch, M. J.; Trucks, G. W.; Schlegel, H. B.; Scuseria, G. E.; Robb, M. A.; Cheeseman, J. R.; Scalmani, G.; Barone, V.; Mennucci, B.; Petersson, G. A.; et al. *Gaussian 09*, Revision D.01; Gaussian, Inc: Wallingford, CT, 2010.

(34) Becke, A. D. Density-functional Thermochemistry. III. The Role of Exact Exchange. *J. Chem. Phys.* **1993**, *98*, 5648−5652.

(35) Stevens, W. J.; Basch, H.; Krauss, M. No Title. *J. Chem. Phys.* **1984**, *81*, 6026−33.

(36) Stevens, W. J.; Krauss, M.; Basch, H.; Jasien, P. G. Relativistic Compact Effective Potentials and Efficient, Shared-Exponent Basis Sets for the Third-, Fourth-, and Fifth-Row Atoms. *Can. J. Chem.* **1992**, *70*, 612−630.

(37) Hehre, W. J.; Radom, L.; Schleyer, P. v. R.; Pople, J. A. *Ab Inition Molecular Orbitals Theory*; Wiley: New York, 1986.

(38) Marenich, A. V.; Cramer, C. J.; Truhlar, D. G. Universal Solvation Model Based on Solute Electron Density and on a Continuum Model of the Solvent Defined by the Bulk Dielectric Constant and Atomic Surface Tensions. *J. Phys. Chem. B* **2009**, *113*, 6378−6396.

(39) Concepcion, J. J.; Jurss, J. W.; Norris, M. R.; Chen, Z.; Templeton, J. L.; Meyer, T. J. Catalytic Water Oxidation by Single-Site Ruthenium Catalysts. *Inorg. Chem.* **2010**, *49*, 1277−1279.

(40) Leigh, V.; Ghattas, W.; Lalrempuia, R.; Müller-Bunz, H.; Pryce, M. T.; Albrecht, M. Synthesis, Photo-, and Electrochemistry of

DOI: 10.1021/jacs.9b01735
J. Am. Chem. Soc. 2019, 141, 6658−6671

Ruthenium Bis(Bipyridine) Complexes Comprising a N-Heterocyclic Carbene Ligand. *Inorg. Chem.* **2013**, *52*, 5395−5402.
(41) Camp, A. M.; Kita, M. R.; Grajeda, J.; White, P. S.; Dickie, D. A.; Miller, A. J. M. Mapping the Binding Modes of Hemilabile Pincer−Crown Ether Ligands in Solution Using Diamagnetic Anisotropic Effects on NMR Chemical Shift. *Inorg. Chem.* **2017**, *56*, 11141−11150.
(42) Matsubara, Y.; Grills, D. C.; Kuwahara, Y. Thermodynamic Aspects of Electrocatalytic CO_2 Reduction in Acetonitrile and with an Ionic Liquid as Solvent or Electrolyte. *ACS Catal.* **2015**, *5*, 6440−6452.
(43) Matsubara, Y. Standard Electrode Potentials for the Reduction of CO_2 to CO in Acetonitrile−Water Mixtures Determined Using a Generalized Method for Proton-Coupled Electron-Transfer Reactions. *ACS Energy Lett.* **2017**, *2*, 1886−1891.
(44) Gennaro, A.; Isse, A. A.; Vianello, E. Solubility and Electrochemical Determination of CO_2 in Some Dipolar Aprotic Solvents. *J. Electroanal. Chem. Interfacial Electrochem.* **1990**, *289*, 203−215.
(45) Savéant, J.-M. *Elements of Molecular and Biomolecular Electrochemistry*; John Wiley & Sons, Inc: Hoboken, NJ, 2006.
(46) Rountree, E. S.; McCarthy, B. D.; Eisenhart, T. T.; Dempsey, J. L. Evaluation of Homogeneous Electrocatalysts by Cyclic Voltammetry. *Inorg. Chem.* **2014**, *53*, 9983−10002.
(47) Walden, A. G.; Miller, A. J. M. Rapid Water Oxidation Electrocatalysis by a Ruthenium Complex of the Tripodal Ligand Tris(2-Pyridyl)Phosphine Oxide. *Chem. Sci.* **2015**, *6*, 2405−2410.
(48) Smieja, J. M.; Benson, E. E.; Kumar, B.; Grice, K. A.; Seu, C. S.; Miller, A. J. M.; Mayer, J. M.; Kubiak, C. P. Kinetic and Structural Studies, Origins of Selectivity, and Interfacial Charge Transfer in the Artificial Photosynthesis of CO. *Proc. Natl. Acad. Sci. U. S. A.* **2012**, *109*, 15646−15650.
(49) Nichols, A. W.; Chatterjee, S.; Sabat, M.; Machan, C. W. Electrocatalytic Reduction of CO_2 to Formate by an Iron Schiff Base Complex. *Inorg. Chem.* **2018**, *57*, 2111−2121.
(50) Chapovetsky, A.; Welborn, M.; Luna, J. M.; Haiges, R.; Miller, T. F.; Marinescu, S. C. Pendant Hydrogen-Bond Donors in Cobalt Catalysts Independently Enhance CO_2 Reduction. *ACS Cent. Sci.* **2018**, *4*, 397−404.
(51) Nakamura, G.; Okamura, M.; Yoshida, M.; Suzuki, T.; Takagi, H. D.; Kondo, M.; Masaoka, S. Electrochemical Behavior of Phosphine-Substituted Ruthenium(II) Polypyridine Complexes with a Single Labile Ligand. *Inorg. Chem.* **2014**, *53*, 7214−7226.
(52) Garg, K.; Matsubara, Y.; Ertem, M. Z.; Lewandowska-Andralojc, A.; Sato, S.; Szalda, D. J.; Muckerman, J. T.; Fujita, E. Striking Differences in Properties of Geometric Isomers of $[Ir(tpy)(ppy)H]^+$: Experimental and Computational Studies of Their Hydricities, Interaction with CO_2, and Photochemistry. *Angew. Chem., Int. Ed.* **2015**, *54*, 14128−14132.
(53) Smieja, J. M.; Benson, E. E.; Kumar, B.; Grice, K. A.; Seu, C. S.; Miller, A. J. M.; Mayer, J. M.; Kubiak, C. P. Kinetic and Structural Studies, Origins of Selectivity, and Interfacial Charge Transfer in the Artificial Photosynthesis of CO. *Proc. Natl. Acad. Sci. U. S. A.* **2012**, *109*, 15646−15650.
(54) Smieja, J. M.; Sampson, M. D.; Grice, K. A.; Benson, E. E.; Froehlich, J. D.; Kubiak, C. P. Manganese as a Substitute for Rhenium in CO_2 Reduction Catalysts: The Importance of Acids. *Inorg. Chem.* **2013**, *52*, 2484−2491.
(55) Oberem, E.; Roesel, A. F.; Rosas-Hernández, A.; Kull, T.; Fischer, S.; Spannenberg, A.; Junge, H.; Beller, M.; Ludwig, R.; Roemelt, M.; et al. Mechanistic Insights into the Electrochemical Reduction of CO_2 Catalyzed by Iron Cyclopentadienone Complexes. *Organometallics* **2019**, *38*, 1236−1247.
(56) Waldie, K. M.; Ostericher, A. L.; Reineke, M. H.; Sasayama, A. F.; Kubiak, C. P. Hydricity of Transition-Metal Hydrides: Thermodynamic Considerations for CO_2 Reduction. *ACS Catal.* **2018**, *8*, 1313−1324.
(57) Francke, R.; Schille, B.; Roemelt, M. Homogeneously Catalyzed Electroreduction of Carbon Dioxide—Methods, Mechanisms, and Catalysts. *Chem. Rev.* **2018**, *118*, 4631−4701.
(58) Wang, Y.; Marquard, S. L.; Wang, D.; Dares, C.; Meyer, T. J. Single-Site, Heterogeneous Electrocatalytic Reduction of CO_2 in Water as the Solvent. *ACS Energy Lett.* **2017**, *2*, 1395−1399.
(59) Sato, S.; Morikawa, T.; Kajino, T.; Ishitani, O. A Highly Efficient Mononuclear Iridium Complex Photocatalyst for CO_2 Reduction under Visible Light. *Angew. Chem., Int. Ed.* **2013**, *52*, 988−992.

DOI: 10.1021/jacs.9b01735
J. Am. Chem. Soc. 2019, 141, 6658−6671